2024 IEEE International Conference on Robotics and Automation (ICRA 2024)
May 13-17, 2024. Yokohama, Japan

Harnessing the Differential Flatness of Monocopter Dynamics for the Purpose of Trajectory Tracking in a Stable Invertible Coaxial Actuated ROtorcraft (SICARO)

Emmanuel Tang[1], Wei Jun Ang[1], Kian Wee Tan[1] and Shaohui Foong[1]

***Abstract*— In this paper, the dynamics of an emerging class of rotating nature-inspired micro aerial vehicles known as the Monocopter is proven and shown to be differentially flat. By exploiting this phenomenon, trajectory tracking can now be implemented on Monocopters via feed-forward terms that are computed per the trajectory. To demonstrate this, a Monocopter in the form of a Stable Invertible Coaxial Actuated ROtorcraft (SICARO) is chosen to harness this approach fully. The SICARO is capable of flying with either side of the wing facing up and this feature determines the craft's direction of rotation about its body Z axis as well. In addition, it has the unique feature of a coaxial motor configuration that allows for a pitching-up moment regardless of the wing side facing up. The feed-forward terms computed are fused into a cascaded nonlinear controller on the craft to ensure its effectiveness in tracking trajectories. Lastly, the flight experiments extend to both sides of the wing to validate this method as being applicable for trajectory tracking for Monocopters such as the SICARO which has an extended range of flying capabilities.**

SUPPLEMENTARY MATERIAL:

Extended flight demonstration of the proposed approach: https://youtu.be/L-e93C53kzM?si=kzKEeshclOOqtlHW
Flight demonstration of how the SICARO flies: https://youtu.be/7y2i45iqZhw?si=Xf79UzpBK9hsByME

I. INTRODUCTION

The Monocopter is a platform with a lot of potential for research. One area that needs further exploration is its performance and limits in trajectory tracking. Currently, there has been little development in controlling the Monocopter for this purpose, and the limitations of its flight envelope are largely unknown. In the early stages of Monocopter research, as detailed in [13, 17, 20, 28, 31], a thorough examination was conducted on the dynamics necessary for both hovering and translational flight. Much of this investigation drew inspiration from the dynamics employed by helicopters [18]. Unlike the comprehensive groundwork laid out by [23] for understanding quadcopter dynamics, the original Monocopter dynamics developed by [20] remain incomplete. This is primarily due to its failure to consider deviations in disk precession rates caused by the interactions between the body's angular momentum and the disk's torque. Additionally, studying the Monocopter's dynamics from its annular frame [18] is an uncommon approach, since most research efforts center around the body frame in their analyses. Subsequent attempts were made by [22] to scrutinize the hovering dynamics from a new perspective whilst recent research was done by [5, 6] to investigate the use of attitude control in separating Monocopters for cooperative flight, and [2] for achieving hovering flight with a biomimetic rotating wing that's passively stable in attitude. Their research highlighted that control schemes significantly influence dynamics, prompting the need to differentiate the craft's control approach during both translational and rotational motion. In the context of translational motion, their studies predominantly centered around minimum velocity trajectories, limited to a confined region within their flight envelope. For trajectories above the order of 1, [1] made advancements in computing feed-forward terms for rotating micro aerial vehicles, however, their platform's flight dynamics mimicked that of a quadcopter which enabled minimal penalization in tracking accuracy whenever the body frame encountered precession. With the premise being set, the focus and contribution of this paper is to address the modeling of the Monocopter that would encompass the property of differential flatness for trajectory tracking. This is combined with a cascaded position to attitude controller for a Monocopter platform like the SICARO, which has an extended flight range capability enabling it to fly on either side of its wing in specific rotations [26]. With this approach, nature-inspired Monocopters can achieve better precision in trajectory tracking whilst reducing energy consumption as compared to existing methods. This is crucial for deployment applications such as surveillance and payload deliveries that may equip them with small and limited battery capacities.

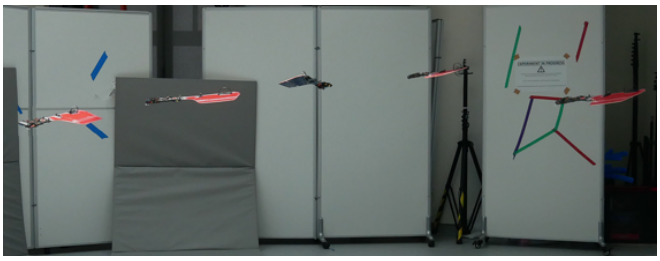

Fig. 1: SICARO flying a circle

II. NOTATION

The reference frames of the Monocopter in Fig.2 consists of the following: $\{\mathbf{X_W}, \mathbf{Y_W}, \mathbf{Z_W}\} \in \mathbb{R}^3$ as the orthonormal basis for the world/inertia frame, $\{\mathbf{X_B}, \mathbf{Y_B}, \mathbf{Z_B}\} \in \mathbb{R}^3$ as the orthonormal basis for the body frame, and $\{\mathbf{X_D}, \mathbf{Y_D}, \mathbf{Z_D}\} \in \mathbb{R}^3$ as the orthonormal basis for the disk frame. Lastly, $\{\mathbf{P_G}, \mathbf{N_G}, \mathbf{S_G}\}$ forms the basis for the gyroscopic frame where $\mathbf{P}$, $\mathbf{N}$, and $\mathbf{S}$ represent the precession, nutation and spin axis

1 Authors are with the Engineering Product Development (EPD) Pillar of Singapore University of Technology and Design (SUTD), 8 Somapah Road, Singapore 487372 (Corresponding e-mail: foongshaohui@sutd.edu.sg)

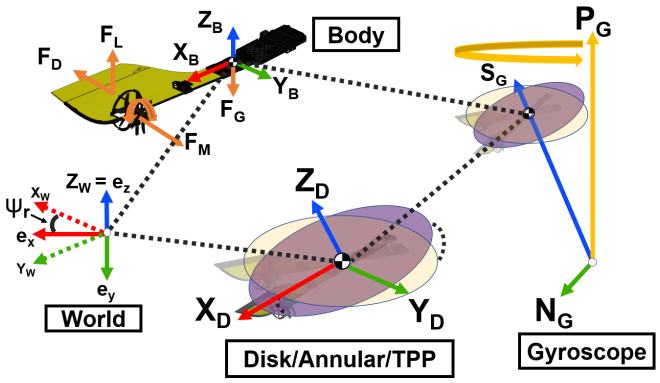

Fig. 2: Entirety of the reference frames used for the Monocopter

respectively. All frames use coordinates in the world frame and $\mathbf{R} = [\mathbf{X}, \mathbf{Y}, \mathbf{Z}] \in SO(3)$ is a rotation matrix where $\mathbf{R_B}$ and $\mathbf{R_D}$ refer to the body and disk's orientation respectively. Lastly, $\mathbf{G}$ as gravity is -9.81 m/s^2 and opposes the direction indicated by $\mathbf{Z_W}$. The origin point for the orthonormal basis of the body and disk is located at the center of gravity and center of rotation of the Monocopter. The state vector of the body and disk is written as $\mathbf{X^B}$ and $\mathbf{X^D}$ consisting of 12 dimensions:

$$\mathbf{X^B} = \begin{bmatrix}\mathbf{P_B} & \boldsymbol{\eta_B} & \mathbf{V_B} & \boldsymbol{\omega_B}\end{bmatrix}, \quad \mathbf{X^D} = \begin{bmatrix}\mathbf{P_D} & \boldsymbol{\eta_D} & \mathbf{V_D} & \boldsymbol{\omega_D}\end{bmatrix}. \tag{1}$$

and the state vector of the gyroscope, $\mathbf{X^G}$, consists of 6 dimensions:

$$\mathbf{X^G} = \begin{bmatrix}\boldsymbol{\eta_G} & \boldsymbol{\omega_G}\end{bmatrix}. \tag{2}$$

where $\mathbf{P} = [P_x, P_y, P_z]$ represents the position, $\mathbf{V}$ represents the linear velocity, and $\boldsymbol{\eta}$ equates to orientation in the form of $[\phi, \theta, \psi]$ that refer to roll, pitch, and yaw which are defined using Euler angles and $\boldsymbol{\omega} = [\omega_x, \omega_y, \omega_z]$ represents angular velocity in the respective frame coordinates depending on the subscript. For the gyroscopic frame, $\boldsymbol{\eta_G}$ equates to orientation where $[\rho_G, \upsilon_G, \psi_G]$ refer to the precession, nutation, and spin of the Monocopter in Euler angles. Lastly, $\boldsymbol{\omega_G} = [\omega_{Gp}, \omega_{Gn}, \omega_{Gs}]$ represents the gyroscopic angular rates where the point of origin for the frame is on the ground.

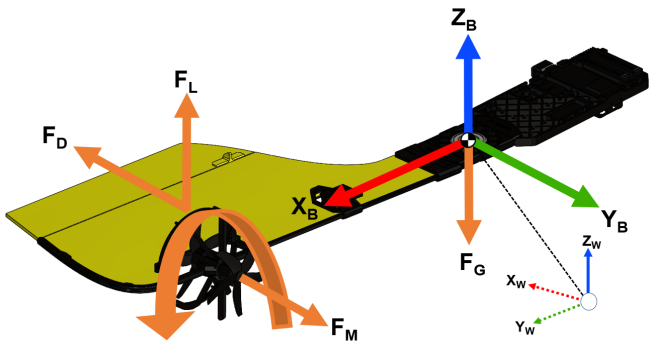

Fig. 3: Body frame

III. Model

A. Body

The body equations of a Monocopter were first developed by [20] to describe its balance of linear and angular momentum by taking in $\mathbf{V_B}$ and $\boldsymbol{\omega_B}$ in $\mathbf{X^B}$.

$$\dot{\mathbf{V}}_\mathbf{B} = \frac{1}{\mathbf{m}}\left(\sum \mathbf{F} - \boldsymbol{\omega_B} \times (\mathbf{m}\mathbf{V_B})\right) \tag{3}$$

$$\dot{\boldsymbol{\omega}}_\mathbf{B} = \mathbf{I}^{-1}\left(\sum \mathbf{M} - \boldsymbol{\omega_B} \times (\mathbf{I}\boldsymbol{\omega_B})\right) \tag{4}$$

$\mathbf{m}$ and $\mathbf{I}$ denote the Monocopter's mass and moment of inertia, respectively. $\mathbf{F}$ and $\mathbf{M}$ are the forces and moments in all axes induced by lift, drag, gravity, and motor thrust as denoted by subscripts shown in Fig.3.

B. Aerodynamic Forces

$$dL = \frac{1}{2} C_L \rho c U^2 \mathrm{d}r \tag{5}$$

$$dD = \frac{1}{2} C_D \rho c U^2 \mathrm{d}r \tag{6}$$

Blade Element Theory from helicopter aerodynamics in [18] was referenced for the lift and drag forces in Eqn.5 and 6. Further information about the equation's corresponding variables for the SICARO and its actual mass and moment of inertia values can be obtained under simulation parameters in [26]. The Total Mass Rotating Force (TMR) which is F_z can be found by integrating Eqn.5 and 6 based on Eqn.8:

$$dF_y = dL \sin\alpha - dD \cos\alpha \tag{7}$$

$$dF_z = dL \cos\alpha - dD \sin\alpha \tag{8}$$

$$\mathrm{TMR} = F_z = \int_0^R \frac{1}{2} C_L \rho c \omega_{Bz}{}^2 r^2 \mathrm{d}r \cdot \cos\alpha \; + \int_0^R \frac{1}{2} C_D \rho c \omega_{Bz}{}^2 r^2 \mathrm{d}r \cdot \sin\alpha \tag{9}$$

The determination of forces in the body frame for $\mathbf{Z_B}$ and $\mathbf{Y_B}$ that come from both drag and lift involves the application of Eqn.7 and 8. Here, α denotes the angle of attack (also known as AOA) of the wing, and σ represents the flap angle employed to induce or reduce lift. A visual representation is briefly provided in Fig.4, while a more comprehensive breakdown of how it correlates with airflow in aerodynamics is explained in [16], and how it applies to Monocopters in [22, 26, 30].

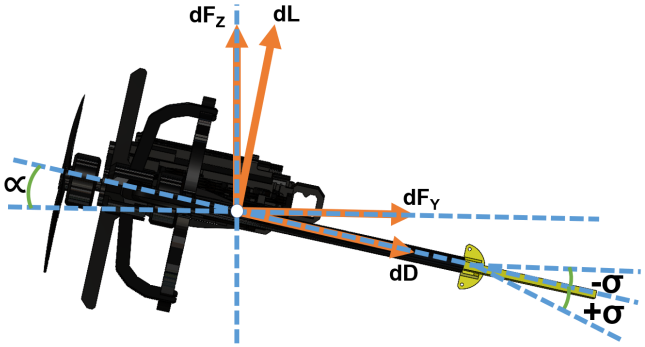

Fig. 4: Monocopter's side profile as referenced in [26]

C. Disk

As the Monocopter spins for flight, its motion is annular as phrased by [18] mimicking a disk, thus, it is crucial to model the craft in this frame. In Fig.5, the purple ellipse represents the disk when it tilts to pitch and the yellow one represents it when it is straight and level. The $\mathbf{X_D}$-$\mathbf{Y_D}$ plane of the disk in reality represents the Tip Path Plane (TPP) [27, 30], which is the plane created by the annular motion of the wing tips during flight and is perpendicular to $\mathbf{Z_D}$.

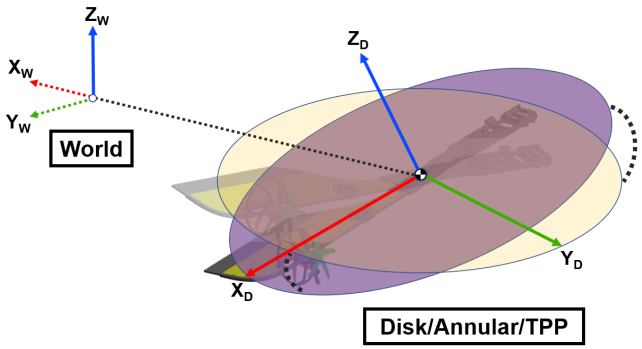

Fig. 5: Disk/Annular frame

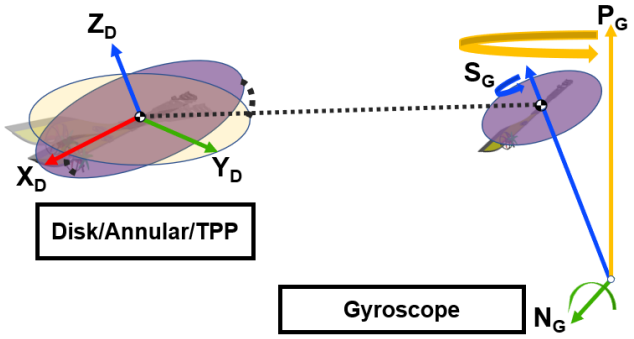

Fig. 6: Gyroscopic frame

D. Gyroscope

As a Monocopter rapidly spins with possibly high disk angles during flight, it will behave like a rotating axisymmetric body such as a spinning top or gyroscope that has the effects of precession visible in its motions. Thus, the final step includes modeling the Monocopter's balance of angular momentum like a gyroscope.

E. Combined Dynamics

The dynamic model of the disk mimics that of a rotating axisymmetric body for non-inertial frames where the principal axes of the disk align with that of the body in Fig.3 but does not rotate together with it about the $\mathbf{Z}$ axis ($\omega_{Dz} \neq \omega_{Bz}$). Given that the disk and body frames are aligned, the aerodynamic components of the disk are classified under the body. The balance of the linear momentum component of the disk adopts an approach that accounts for drag induced by the spinning motion of the body as similarly developed by [9, 19] for the rotors in quadcopters. Thus, with the balance of angular momentum including the gyroscopic dynamics, the equations for the combined dynamics are the following:

$$\dot{\mathbf{P_D}} = \mathbf{V_D} \tag{10}$$

$$\dot{\mathbf{V_D}} = C\mathbf{Z_D} - (\mathbf{R}_D\mathbf{D_D}\mathbf{R}_D^T)\mathbf{V_D} - \mathbf{G}\mathbf{Z_W} \tag{11}$$

$$\dot{\mathbf{R_D}} = \mathbf{R_D} \cdot \hat{\boldsymbol{\omega}}_\mathbf{D} \tag{12}$$

$$\dot{\boldsymbol{\omega}}_\mathbf{D} = \mathbf{I}^{-1}(\boldsymbol{\tau_D} - \boldsymbol{\omega_D} \times (\mathbf{I}\boldsymbol{\omega_D})) \tag{13}$$

$$\begin{aligned}\boldsymbol{\tau}_{Gn} \equiv \boldsymbol{\tau}_{Dy} = \hat{I}_{xx}(\dot{\omega_{Gn}} - {\omega_{Gp}}^2 \sin\upsilon_G \cos\upsilon_G) \\ +\hat{I}_{zz}\omega_{Gp}\sin\upsilon_G(\omega_{Gp}\cos\upsilon_G + \omega_{Bz})\end{aligned} \tag{14}$$

where $\hat{I}_{xx}$ and $\hat{I}_{zz}$ refer to the mass moment of inertia about $\mathbf{X_B}$ and $\mathbf{Z_B}$ of the body and the drag term $\mathbf{D_D}$ in Eqn.11 is presented in the form of a diagonal matrix, $\hat{\boldsymbol{\omega}}_\mathbf{D}$ refers to the skew-symmetric matrix containing values from $\boldsymbol{\omega_D}$, and the collective thrust term C corresponds to the force required along $\mathbf{Z_D}$ which given that $\mathbf{Z_D} \times \mathbf{Z_B} = 0$, this implies $C = F_Z$ in Eqn.9. Because of how the frames are connected as seen in Fig.6, relationships can be established that allow certain terms to be shared across frames:

$$\begin{aligned}\because \mathbf{N_G} \times \mathbf{Y_D} = 0 \implies \boldsymbol{\tau}_{Gn} \equiv \boldsymbol{\tau}_{Dy} \\ \therefore \{\upsilon_G \equiv \theta_D, \quad \omega_{Gn} \equiv \omega_{Dy}, \quad \dot{\omega_{Gn}} \equiv \dot{\omega_{Dy}}\} \\ \text{s.t.} \quad \omega_{Gs} \neq \omega_{Bz}\end{aligned} \tag{15}$$

Because $\mathbf{N_G}$ and $\mathbf{Y_D}$ are collinear in Eqn.15, $\boldsymbol{\tau}_{Gn}$ being the nutation torque is equivalent to $\boldsymbol{\tau}_{Dy}$ where based on the derivations from [15], Eqn.14 is defined for axisymmetric spinning bodies.

IV. Differential Flatness

In this section, it will be shown that the combined dynamics from Eqn.10 to 14 with two control inputs is differentially flat. In a differentially flat system, the referenced states defined as $\mathbf{X^r} = [\mathbf{P_D^r}, \mathbf{V_D^r}, \mathbf{R_D^r}, \boldsymbol{\omega_D}^\mathbf{r}, {\omega_{Bz}}^\mathbf{r}, {\omega_{Gp}}^\mathbf{r}, {\omega_{Gn}}^\mathbf{r}, {\upsilon_G}^\mathbf{r}]$ and the referenced control inputs defined as $\mathbf{U^r} = [C^\mathbf{r}, \boldsymbol{\tau}_{Gn}^\mathbf{r}]$ can be expressed as algebraic functions of a select group of 4 flat outputs and a finite amount of time derivatives based on [12, 21]. These flat outputs like [9, 10, 25] are chosen to be the referenced position of the disk and its referenced heading. The vector y for the flat outputs is defined in Eqn.16, where this and Eqn.17 is true iff the smooth functions in Eqn.18 and 19 exists:

$$y = \begin{bmatrix} P_{rx} & P_{ry} & P_{rz} & \psi_r \end{bmatrix}. \tag{16}$$

$$y = f_y(\mathbf{P_D^r}, \mathbf{V_D^r}, \mathbf{R_D^r}, \boldsymbol{\omega_D}^\mathbf{r}, {\omega_{Bz}}^\mathbf{r}, {\omega_{Gp}}^\mathbf{r}, {\omega_{Gn}}^\mathbf{r}, {\upsilon_G}^\mathbf{r}, C^\mathbf{r}, \boldsymbol{\tau}_{Gn}^\mathbf{r}) \tag{17}$$

$$\begin{aligned}[\mathbf{P_D^r}, \mathbf{V_D^r}, \mathbf{R_D^r}, \boldsymbol{\omega_D}^\mathbf{r}, {\omega_{Bz}}^\mathbf{r}, {\omega_{Gp}}^\mathbf{r}, {\omega_{Gn}}^\mathbf{r}, {\upsilon_G}^\mathbf{r}] \\ = f_x(y, \dot{y}, \ddot{y}, \dddot{y}, \ddddot{y}, ...)\end{aligned} \tag{18}$$

$$[C^\mathbf{r}, \boldsymbol{\tau}_{Gn}^\mathbf{r}] = f_u(y, \dot{y}, \ddot{y}, \dddot{y}, \ddddot{y}, ...) \tag{19}$$

The variables P_{rx}, P_{ry}, P_{rz} in Eqn.16 represent Cartesian world coordinates and the variable ψ_r represents heading about $\mathbf{Z_W}$ that are taken from a referenced trajectory.

A. Disk's Orientation

In this section, the formulation as referenced from [9] would describe and show that the orientation $\mathbf{R_D}$ can be expressed as a function of the flat outputs. For the unique case of a Monocopter, an intermediary orthonormal basis comprising of unit vectors $\{e_x, e_y, e_z\}$ as shown in Fig.2 is created and aligned with the disk's heading ψ_D despite the yaw on the $\mathbf{X_W}$-$\mathbf{Y_W}$ plane due to ψ_r shown in Fig.2. As the Monocopter can adhere to ψ_r digitally without any actuation or physical motion, the referenced heading can easily be enforced whilst the axis of $\mathbf{X_D}$ remain collinear with e_x when projected onto the $\mathbf{X_W}$-$\mathbf{Y_W}$ plane. The respective axis in the orientation can be isolated and found by first multiplying both sides of Eqn.11 by its transpose where $\mathbf{A_D} = \dot{\mathbf{V}}_\mathbf{D}$.

$$\begin{aligned}\mathbf{A_D} + \mathbf{G}\mathbf{Z_W} \\ = C\mathbf{Z_D} - (\mathbf{X_D}D_x{\mathbf{X_D}}^T + \mathbf{Y_D}D_y{\mathbf{Y_D}}^T + \mathbf{Z_D}D_z{\mathbf{Z_D}}^T)\mathbf{V_D}\end{aligned} \tag{20}$$

For $\mathbf{X_D}$:

$$\mathbf{X_D}^T(\mathbf{A_D} + D_x\mathbf{V_D} + \mathbf{GZ_W}) = 0 \tag{21}$$

For $\mathbf{Y_D}$:

$$\mathbf{Y_D}^T(\mathbf{A_D} + D_y\mathbf{V_D} + \mathbf{GZ_W}) = 0 \tag{22}$$

In the case of a Monocopter, the drag coefficients (D_x, D_y) in $\mathbf{D_D}$ are equivalent along $\mathbf{X_W}$ and $\mathbf{Y_W}$ because of the symmetrical profile of the disk.

$$\begin{gathered} \because D_x = D_y \\ \therefore \mathbf{X_D}^T\kappa = \mathbf{Y_D}^T\kappa, \quad \kappa = \mathbf{A_D} + D_x\mathbf{V_D} + \mathbf{GZ_W} \end{gathered} \tag{23}$$

Because of the orthonormal constraints when solving for $\mathbf{R_D}$, the cross product of κ and the basis vectors of the intermediary orthonormal basis is formed and normalized to solve for the respective vectors:

$$\mathbf{X_D} = \frac{e_y \times \kappa}{||e_y \times \kappa||}, \quad \mathbf{Y_D} = \frac{\kappa \times \mathbf{X_D}}{||\kappa \times \mathbf{X_D}||}, \quad \mathbf{Z_D} = \mathbf{X_D} \times \mathbf{Y_D} \tag{24}$$

B. Disk's Collective Thrust And Body Yaw Rate ω_{Bz}

To solve for the collective thrust C, $\mathbf{Z_D}$ from Eqn.24 is used. Given C = F_Z in Eqn.9, ω_{Bz} can be found.

$$\mathbf{Z_D}^T(\mathbf{A_D} + D_z\mathbf{V_D} + \mathbf{GZ_W}) = C \tag{25}$$

C. Disk Rates

Next, to solve for the rates $\boldsymbol{\omega_D}$ of the disk as a function of the flat outputs, jerk $\mathbf{J_D}$ is introduced as part of the following formulation where $\mathbf{J_D} = \dot{\mathbf{A_D}}$:

$$\begin{aligned} \mathbf{J_D} = C(\omega_{Dy}\mathbf{X_D} - \omega_{Dx}\mathbf{Y_D}) - \mathbf{R_D}((\hat{\boldsymbol{\omega}}_\mathbf{D}\mathbf{D_D} + \mathbf{D_D}\hat{\boldsymbol{\omega}}_\mathbf{D}{}^T)\mathbf{R_D}^T\mathbf{V_D} \\ +\mathbf{D_D}\mathbf{R_D}^T\mathbf{A_D}) + \dot{C}\mathbf{Z_D} \end{aligned} \tag{26}$$

To solve for the disk rates, the method used in Eqn.21 and 22 on Eqn.20 can be applied to Eqn.26. Therefore,

$$\omega_{Dx} = \frac{\mathbf{Y_D}{}^T\mathbf{J_D} + D_y\mathbf{Y_D}^T\mathbf{A_D}}{(-C - D_y\mathbf{Z_D}^T\mathbf{V_D} - D_z\mathbf{Z_D}^T\mathbf{V_D})} \tag{27}$$

$$\omega_{Dy} = \frac{\mathbf{X_D}{}^T\mathbf{J_D} + D_x\mathbf{X_D}^T\mathbf{A_D}}{(C + D_x\mathbf{Z_D}^T\mathbf{V_D} + D_x\mathbf{X_D}^T\mathbf{V_D} - D_z\mathbf{Z_D}^T\mathbf{V_D})} \tag{28}$$

Due to the effortless requirement to rotate about $\mathbf{Z_D}$ to ψ_r digitally, the equation for ω_{Dz} and subsequently $\dot{\omega_{Dz}}$ is not necessary as the yaw is approximately instant.

D. Disk Angular Acceleration and Torque

Lastly, to solve for the disk body acceleration as a function of the flat outputs, snap $\mathbf{S_D}$ is invoked in the formulation below with $\mathbf{S_D} = \dot{\mathbf{J_D}}$.

$$\begin{aligned} \mathbf{S_D} = \ddot{C}\mathbf{Z_D} + 2\dot{C}\mathbf{R_D}\hat{\boldsymbol{\omega}}_\mathbf{D}e_z + C(\mathbf{R_D}\hat{\boldsymbol{\omega}}_\mathbf{D}^2e_z + \mathbf{R_D}\hat{\dot{\boldsymbol{\omega}}}_\mathbf{D}e_z) \\ -\mathbf{R_D}(\hat{\dot{\boldsymbol{\omega}}}_\mathbf{D}\mathbf{D_D} + \mathbf{D_D}\hat{\dot{\boldsymbol{\omega}}}_\mathbf{D}^T)\mathbf{R_D}^T\mathbf{V_D} - \boldsymbol{\beta} \end{aligned} \tag{29}$$

where:

$$\begin{aligned} \boldsymbol{\beta} = \mathbf{R_D}(\hat{\boldsymbol{\omega}}_\mathbf{D}{}^2\mathbf{D_D} + \mathbf{D_D}(\hat{\boldsymbol{\omega}}_\mathbf{D}{}^T)^2 + 2\hat{\boldsymbol{\omega}}_\mathbf{D}\mathbf{D_D}\hat{\boldsymbol{\omega}}_\mathbf{D}{}^T)\mathbf{R_D}^T\mathbf{V_D} \\ +2\mathbf{R_D}(\hat{\boldsymbol{\omega}}_\mathbf{D}\mathbf{D_D} + \mathbf{D_D}\hat{\boldsymbol{\omega}}_\mathbf{D}{}^T)\mathbf{R_D}^T\mathbf{A_D} + \mathbf{R_D}\mathbf{D_D}\mathbf{R_D}^T\mathbf{J_D} \end{aligned} \tag{30}$$

To solve for the disk body acceleration, the method in Eqn.21 and 22 is applied again. Therefore,

$$\dot{\omega_{Dx}} = \frac{-\mathbf{Y_D}{}^T\mathbf{S_D} + C\omega_{Dy}\omega_{Dz} - 2\dot{C}\omega_{Dx} - \mathbf{Y_D}^T\boldsymbol{\beta}}{(C + \mathbf{Z_D}^TD_y\mathbf{V_D} - \mathbf{Z_D}^TD_z\mathbf{V_D})} \tag{31}$$

And, $\dot{\omega_{Dy}}$

$$= \frac{\mathbf{X_D}{}^T\mathbf{S_D} - 2\dot{C}\omega_{Dy} - C\omega_{Dz}\omega_{Dx} + \mathbf{X_D}^T\boldsymbol{\beta} + \dot{\omega_{Dx}}(Dy\mathbf{Y_D}^T\mathbf{V_D})}{(C + \mathbf{Z_D}^TD_x\mathbf{V_D} + D_x\mathbf{X_D}^T\mathbf{V_D} - \mathbf{Z_D}^TD_z\mathbf{V_D})} \tag{32}$$

By substituting $\dot{\omega_D}$ into Eqn.13, $\boldsymbol{\tau}_D$ can be obtained. With the rate of change in the collective thrust C being:

$$\dot{C} = \mathbf{Z_D}{}^T\mathbf{S_D} + \mathbf{Z_D}^TD_z\mathbf{A_D} \tag{33}$$

E. Gyroscopic Nutation Angle

It is important to match the number of controllable axes between the disk and the gyroscopic frame. Thus, setpoints in the $\mathbf{X_W}$-$\mathbf{Y_W}$ plane are converted to polar coordinates:

$$R_r = \sqrt{P_{rx}^2 + P_{ry}^2}, \quad \psi_r = \arctan 2(P_{ry}, P_{rx}) \tag{34}$$

Upon which, the line formed from R_r in Eqn.34 would now be collinear with e_x because the intermediary orthonormal basis always deviates by ψ_r as previously established, which is now the polar angle in Eqn.34. The rotation of the disk about $\mathbf{Z_D}$ can be digitally adjusted without any added actuation to inform when the flaps should actuate based on ψ_r. Because of this, the Monocopter only needs to pitch forward in the direction of e_x at all times which requires only one torque input. This single torque input about $\mathbf{Y_D}$ of the disk frame can also be classified as the torque input about the nutation axis $\mathbf{N_G}$ based on Eqn.15 and 14. Thus, the nutation angle υ_G can be expressed as a function of the flat outputs:

$$\upsilon_G = \arccos\left(\frac{e_x \cdot \kappa}{||e_x||||\kappa||}\right) \tag{35}$$

With no roll commands issued about $\mathbf{X_D}$ with this approach, the precession angle allows the craft to bank against the centrifugal force where the lift generated by the Monocopter serves as a centripetal force to counter it during high-speed turns.

F. Gyroscopic Nutation Rates, Angular Acceleration, and Torque

The nutation rate ω_{Gn} can be expressed as a function of the flat outputs based on the relationship from Eqn.15 and the nutation angular acceleration being:

$$\{\dot{\omega}_{Gn} \equiv \dot{\omega}_{Dy}, \quad \boldsymbol{\tau}_{Gn} \equiv \boldsymbol{\tau}_{Dy}\} \quad | \quad \omega_{Gn} \equiv \omega_{Dy} \tag{36}$$

Because of the relationship in Eqn.14, 15, and 36, the nutation torque $\boldsymbol{\tau}_{Gn}$ can also be expressed as a function of the flat outputs with the above equivalence. Thus, with the unified term in Eqn.14, the precession rate ω_{Gp} can be obtained as well subjected to the following gyroscopic constraints:

$$|\omega_{Gp}| << |\omega_{Bz}|, \quad |\omega_{Gp}| > |\dot{\psi_r}| \tag{37}$$

G. Exceptional Instances

$$\frac{\kappa \times e_x}{||\kappa \times e_x||} = \infty \quad | \quad \kappa \times e_x = 0 \tag{38}$$

In the case where Eqn.38 is encountered, an undefined solution is produced when e_x is aligned with κ.

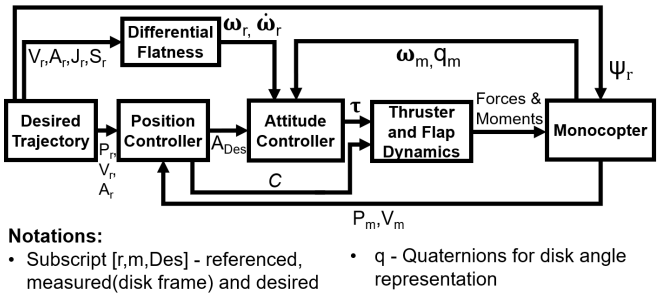

Fig. 7: Control diagram

V. Control

For the Monocopter to follow a reference trajectory, a cascaded outer-to-inner loop control structure is employed using real-time state feedback, along with feed-forward elements obtained from the Monocopter's differential flatness property. Much like [4, 8, 9], the outer-loop consists of a position controller and produces desired values in terms of orientation, collective thrust, angular rates, and angular acceleration which are then fed into an inner-loop attitude controller. A_{Des} comprises the desired acceleration terms in all 3 axes for the disk and is cascaded from the outer to inner loop in Fig.7. The computation of it is standard and involves feedback terms in a PD controller as presented in [9, 25]. The attitude controller in Fig.7 also follows the foundation of [7] and the work of [4, 14] of which in the case of the Monocopter, the feedforward terms are the referenced disk's angular rates and angular acceleration as presented in section VI. Both controllers require gains where their respective values of $\{\mathbf{K_P}, \mathbf{K_D}\} > 0$ and the feedback matrices of the disk's position $\mathbf{P_D}$ and orientation $\boldsymbol{\eta_D}$ are presented as the following:

$$\mathbf{P_D} = \begin{bmatrix} \sqrt{P_{Dx}^2 + P_{Dy}^2} & 0 & P_{Dz} \end{bmatrix}^T, \quad \boldsymbol{\eta_D} = \begin{bmatrix} 0 & \theta_D & \psi_D \end{bmatrix}^T. \tag{39}$$

where $\psi_D = \psi_r$ and the format extended to $\mathbf{V_D}$ and $\boldsymbol{\omega_D}$ as well. Given that $\mathbf{X_D}$ is not required, it is replaced with e_x for Eqn.28 and 32. The remaining desired orientation and collective thrust can be achieved via the following:

$$\mathbf{Z_D} = \frac{A_{Des}}{||A_{Des}||}, \quad \mathbf{Y_D} = \frac{\mathbf{Z_D} \times e_x}{||\mathbf{Z_D} \times e_x||}, \quad C = \mathbf{Z_D^T} A_{Des} \tag{40}$$

VI. Flight Experiments

A. Generation Of Flat Outputs

Eqn.41 presents the calculus of variations approach as used by [11] for hand coordination and [25] for quadcopters to mathematically generate the flat outputs y and its derivatives [12, 21] based on the properties of the flight trajectory chosen and the derivative to minimize.

$$\begin{aligned} y(1:3) = \min_{x(t),y(t),z(t)} & \int_0^T ((x^k)^2 + (y^k)^2 + (z^k)^2)\, dt \\ \text{s.t.} \quad & x^*(t), y^*(t), z^*(t) \in C^k(0,T), \quad k \in \mathbb{Z}^+ \end{aligned} \tag{41}$$

B. Experiment Configuration

The experiment was carried out using the SICARO platform, featuring a wingspan measuring 340mm. This platform employs a coaxial setup with two BetaFPV 1506 3000KV motors paired with 5-bladed propellers that are 3 inches wide in disk diameter and made from Gemfan. The Hyperion DS09 was used as the servo and it was controlled by an isolated ESP32-S3 micro-controller unit (MCU), as depicted in the overall diagram in Fig.8. Furthermore, power was supplied to the system through two BetaFPV 300mah batteries arranged in a series configuration (4S), regulated to 5V direct (DC). As a fail-safe measure, a radio receiver was included in the event a human pilot needed to assume control. To indicate which side of the wing is facing up, the wing is colored in Fig.9 where the red side would be the craft rotating counter-clockwise about $\mathbf{Z_B}$ and the blue would be rotating clockwise. For an additional in-depth understanding of the design of SICARO and its components, kindly refer to [26]. In the transmission setup, the MCU receives control input at 100Hz over telemetry from an external computing unit operating at 100Hz as well. The controllers as mentioned operate in this unit where it receives position and angular feedback of the craft at 360Hz from an Optitrack motion-capturing system.

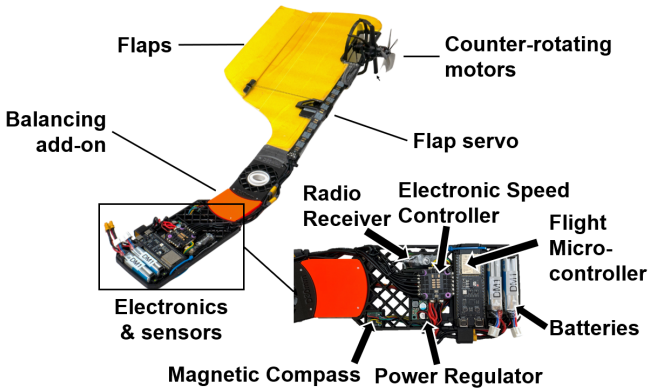

Fig. 8: Hardware configuration of SICARO

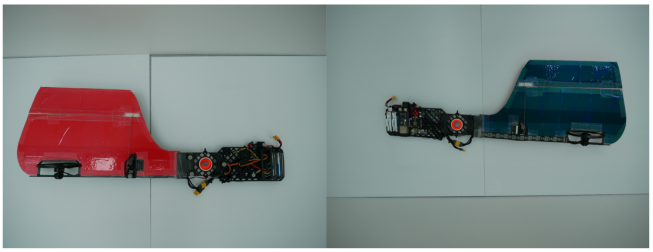

Fig. 9: Red for counter-clockwise rotation, blue for clockwise

Fig. 10: SICARO flying on both sides

C. Trajectory

The trajectory that the SICARO would fly to demonstrate this approach is a circle of 0.8-meter radius and the goal is to track this trajectory at 1m/s whilst maintaining an altitude of 1.5 meters over a given time sequence. Both sides of

the SICARO will be flown to ascertain the effectiveness of this approach. With regards to the highest order in the setpoints for the flat outputs, jerk was chosen because the control inputs in torque for the SICARO require it. The drag coefficients in $\mathbf{D_D}$ were obtained as initial values from [24] through their numerical findings. To ascertain the necessity of this approach, a conventional PD position controller as used by [3, 29] was implemented to traverse the circle carefully. Due to the control method being rudimentary, it was unable to account for the primary precession exerted on the disk as seen in Fig.6. The result is the inability to complete the circle smoothly due to the heavy interruptions of precession that manifested in the form of trochoids as seen in Fig.11.

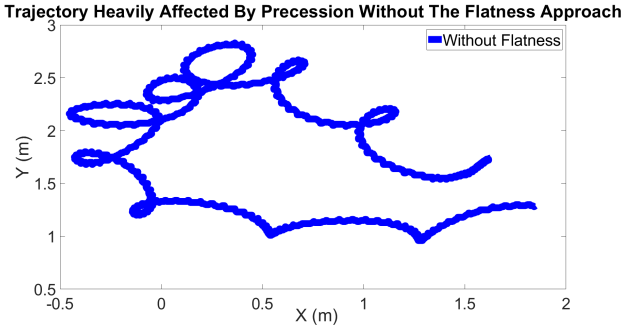

Fig. 11: Failed circle trajectory with significantly visible trochoids from 2D perspective

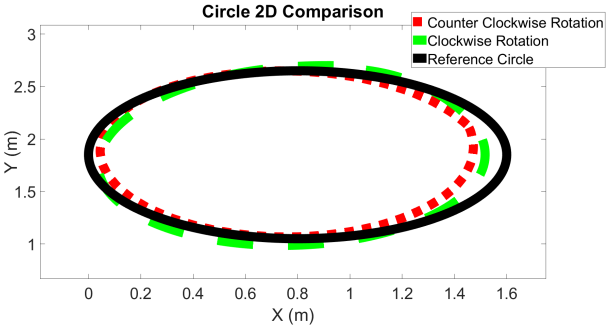

Fig. 12: Circle trajectory from 2D perspective

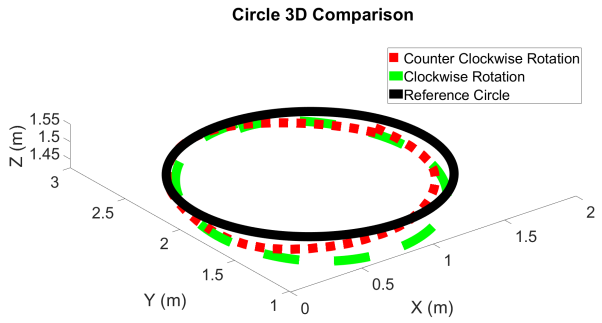

Fig. 13: Circle trajectory from 3D perspective

D. Performance

As observed in Fig.12 and 13, the SICARO was able to track the circle smoothly on both sides when flown using the new flatness-based approach with no signs of precession-induced trochoids as observed in Fig.11 in its course. The absolute position error in Fig.14 captured for all 3 axes on both sides was consistent and the $\mathbf{X_W}$-$\mathbf{Y_W}$ components in the velocity graph in Fig.15 were

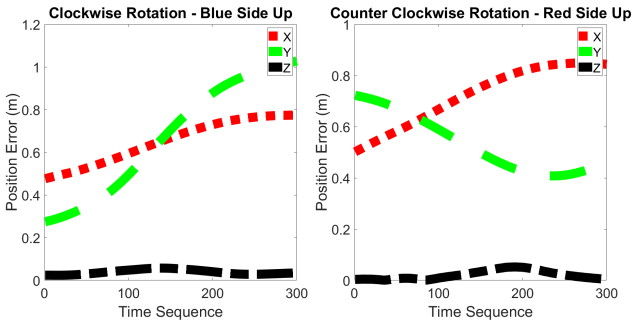

Fig. 14: Absolute position error

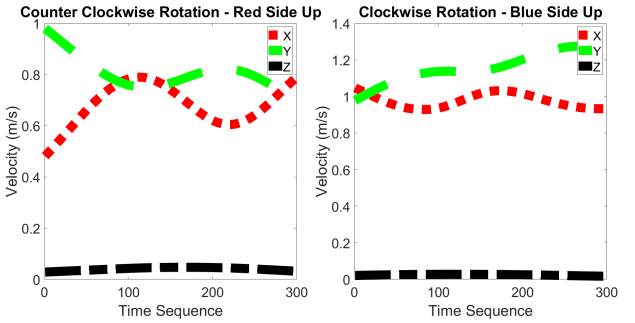

Fig. 15: Absolute velocity

approximately near 1m/s which was the intended velocity designated for the SICARO to traverse at.

E. Discussion

The cause for positional inaccuracy at times in Fig.14 during the trajectory is owed to the fact that the entire system is unable to eradicate primary precession forces completely at all times due to the limited control inputs in this severely under-actuated platform. Despite this constraint, this approach has enabled it to track a circle smoothly without significantly visible trochoids as compared[1] to the failed attempt without this approach in Fig.11. Furthermore, unlike the current approaches in [3, 5, 29] that primarily involve small to negligible body angle movements, this method fully enables the Monocopter to traverse along smooth and continuous trajectories using disk angle motions.

VII. Conclusion

In summary, this approach offers a novel solution, empowering the Monocopter to navigate continuous trajectories through controlled disk angle motions without exhibiting trochoids, a significant advancement in Monocopter technology. For future work, the authors intend to further explore methods to better mitigate precession forces with better airframe designs as well as modern and optimal control strategies. These new implementations would pit against this current approach in a review to verify and validate the necessary adjustments required for better trajectory tracking and transition.

VIII. Acknowledgements

This research is supported by the Ministry of Education, Singapore, under its Academic Research Fund Tier 2 (MOE-T2EP50123-0004) and SUTD Kickstarter Initiative (SKI 2021_03_08).

[1]The authors' decision for isolating the flight in Fig.11 was made to highlight the significant tracking difference without the proposed approach

REFERENCES

[1] Songnan Bai and Pakpong Chirarattananon. Splitflyer air: A modular quadcopter that disassembles into two bicopters mid-air. *IEEE/ASME Transactions on Mechatronics*, 27(6):4729–4740, 2022.

[2] Songnan Bai, Qingning He, and Pakpong Chirarattananon. A bioinspired revolving-wing drone with passive attitude stability and efficient hovering flight. *Science Robotics*, 7(66):eabg5913, 2022.

[3] Hitesh Bhardwaj, Shane Kyi Hla Win, Luke Soe Thura Win, Danial Sufiyan, and Foong Shaohui. P.i.d. based sliding mode control of asynchronous multi-actuator monocopter. In *2021 IEEE/ASME International Conference on Advanced Intelligent Mechatronics (AIM)*, pages 239–246, 2021.

[4] Dario Brescianini, Markus Hehn, and Raffaello D'Andrea. Nonlinear quadrocopter attitude control: Technical report. Technical report, ETH Zurich, 2013.

[5] Xinyu Cai, Shane Kyi Hla Win, Hitesh Bhardwaj, and Shaohui Foong. Modeling, control and implementation of adaptive reconfigurable rotary wings (arrows). *IEEE/ASME Transactions on Mechatronics*, 2023.

[6] Xinyu Cai, Shane Kyi Hla Win, Luke Soe Thura Win, Danial Sufiyan, and Shaohui Foong. Cooperative modular single actuator monocopters capable of controlled passive separation. In *2022 International Conference on Robotics and Automation (ICRA)*, pages 1989–1995. IEEE, 2022.

[7] James Diebel et al. Representing attitude: Euler angles, unit quaternions, and rotation vectors. *Matrix*, 58(15-16):1–35, 2006.

[8] Matthias Faessler, Flavio Fontana, Christian Forster, and Davide Scaramuzza. Automatic re-initialization and failure recovery for aggressive flight with a monocular vision-based quadrotor. In *2015 IEEE international conference on robotics and automation (ICRA)*, pages 1722–1729. IEEE, 2015.

[9] Matthias Faessler, Antonio Franchi, and Davide Scaramuzza. Differential flatness of quadrotor dynamics subject to rotor drag for accurate tracking of high-speed trajectories. *IEEE Robotics and Automation Letters*, 3(2):620–626, 2018.

[10] Jeff Ferrin, Robert Leishman, Randy Beard, and Tim McLain. Differential flatness based control of a rotorcraft for aggressive maneuvers. In *2011 IEEE/RSJ International Conference on Intelligent Robots and Systems*, pages 2688–2693, 2011.

[11] Tamar Flash and Neville Hogan. The coordination of arm movements: an experimentally confirmed mathematical model. *Journal of neuroscience*, 5(7):1688–1703, 1985.

[12] Michel Fliess, Jean Lévine, Philippe Martin, and Pierre Rouchon. Flatness and defect of non-linear systems: introductory theory and examples. *International journal of control*, 61(6):1327–1361, 1995.

[13] Kingsley Fregene and Cortney L Bolden. Dynamics and control of a biomimetic single-wing nano air vehicle. In *Proceedings of the 2010 american control conference*, pages 51–56. IEEE, 2010.

[14] Emil Fresk and George Nikolakopoulos. Full quaternion based attitude control for a quadrotor. In *2013 European control conference (ECC)*, pages 3864–3869. IEEE, 2013.

[15] Donald T Greenwood. *Principles of dynamics*, volume 21. Prentice-Hall Englewood Cliffs, NJ, 1988.

[16] Snorri Gudmundsson. *General aviation aircraft design: Applied Methods and Procedures*. Butterworth-Heinemann, 2013.

[17] James Houghton and Woody Hoburg. Fly-by-wire control of a monocopter. *Massachusetts Institute of Technology, Project Report*, 2008.

[18] Stewart Houston. Principles of helicopter aerodynamics. jg leishman. cambridge university press, the edinburgh building, cambridge cb2 2ru, uk. 2000. 496pp. illustrated.£ 60 isbn 0-521-66060-2. *The Aeronautical Journal*, 104(1038):390–390, 2000.

[19] Jean-Marie Kai, Guillaume Allibert, Minh-Duc Hua, and Tarek Hamel. Nonlinear feedback control of quadrotors exploiting first-order drag effects. *IFAC-PapersOnLine*, 50(1):8189–8195, 2017.

[20] Andreas Kellas. *The guided samara: design and development of a controllable single-bladed autorotating vehicle*. PhD thesis, Massachusetts Institute of Technology, 2007.

[21] Jean Levine. *Analysis and control of nonlinear systems: A flatness-based approach*. Springer Science & Business Media, 2009.

[22] Jun En Low, Ying Hong Pheh, and Shaohui Foong. Analysis of wing twist effects on hover flight dynamics of a single rotor aerial craft. In *2016 IEEE International Conference on Advanced Intelligent Mechatronics (AIM)*, pages 323–328, 2016.

[23] Robert Mahony, Vijay Kumar, and Peter Corke. Multirotor aerial vehicles: Modeling, estimation, and control of quadrotor. *IEEE Robotics Automation Magazine*, 19(3):20–32, 2012.

[24] Gašper Matič, Marko Topič, and Marko Jankovec. Mathematical model of a monocopter based on unsteady blade-element momentum theory. *Journal of Aircraft*, 52(6):1905–1913, 2015.

[25] Daniel Mellinger and Vijay Kumar. Minimum snap trajectory generation and control for quadrotors. In *2011 IEEE International Conference on Robotics and Automation*, pages 2520–2525, 2011.

[26] Emmanuel Tang, Wei Jun Ang, Kian Wee Tan, and Shaohui Foong. Design and control of a stable invertible coaxial actuated rotorcraft (sicaro). In *2023 IEEE/ASME International Conference on Advanced Intelligent Mechatronics (AIM)*, pages 255–262, 2023.

[27] Lorenzo Trainelli, CARLO RIBOLDI, Mattia Bucari, et al. Observing the angle of attack of the tip-path plane from rotor blade measurements. In *41st European Rotorcraft Forum*, pages 1190–1201. Curran Associates, 2015.

[28] Evan R Ulrich, Imraan Faruque, Jared Grauer, Darryll J Pines, J Sean Humbert, and James E Hubbard Jr. Control model for robotic samara: Dynamics about a coordinated helical turn. *Journal of guidance, control, and dynamics*, 33(6):1921–1927, 2010.

[29] Luke Soe Thura Win, Shane Kyi Hla Win, Danial Sufiyan, Gim Song Soh, and Shaohui Foong. Achieving efficient controlled flight with a single actuator. In *2020 IEEE/ASME International Conference on Advanced Intelligent Mechatronics (AIM)*, pages 1625–1631. IEEE, 2020.

[30] Shane Kyi Hla Win, Luke Soe Thura Win, Danial Sufiyan, and Shaohui Foong. Design and control of the first foldable single-actuator rotary wing micro aerial vehicle. *Bioinspiration & Biomimetics*, 16(6):066019, 2021.

[31] Harold Youngren, Steve Jameson, and Brian Satterfield. Design of the samarai monowing rotorcraft nano air vehicle. In *Proceedings of the American Helicopter Society AHS 65th Annual Forum and Technology Display*, 2009.